Time-lapse S-wave tomography at a test dike with changing water levels

Minato, Shohei; Ghose, Ranajit

DOI
10.1190/geo2024-0702.1

Publication date
2025

Document Version
Final published version

Published in
Geophysics

GEOPHYSICS, VOL. 90, NO. 3 (MAY-JUNE 2025); P. KS61–KS73, 19 FIGS., 1 TABLE.
10.1190/GEO2024-0702.1

Time-lapse S-wave tomography at a test dike with changing water levels

Shohei Minato[1] and Ranajit Ghose[2]

ABSTRACT

Although seismic methods using S waves can offer high-resolution images of the shallow soil layers, the use of body S-wave tomography for near-surface water monitoring remains underexplored, and the quantitative interpretation of any observed changes in S-wave velocity (V_S) in the field conditions is challenging. We conduct a time-lapse S-wave tomography experiment on a field-scale test dike with controlled water levels, allowing for detailed examination of how V_S responds to water infiltration. Our results demonstrate that V_S decreases progressively, starting from the high-water-side slope and extending across the dike, as the water level rises, with the most significant changes occurring in the sand body and not in the clay cover. The maximum reduction in V_S is approximately 40–60 m/s, corresponding to approximately 25%–30% reduction from the initial condition. We use the squared velocity ratio to evaluate the relative contributions of bulk density and shear modulus to V_S changes. In the initially unsaturated zone, both factors contribute significantly to the observed V_S changes as the zone becomes fully saturated. In fully saturated zones, we assess the changes in the effective stress using the squared V_S ratio. Although the low-water side of the dike shows stress changes that are consistent with numerical modeling, the high-water side shows larger stress changes than expected, possibly due to excess pore pressure during the dynamic flow conditions. These findings highlight the potential of body S-wave tomography for high-resolution, near-surface hydrologic monitoring, and provide insights into the complex interactions between physical properties that influence V_S changes under varying water levels in field environments.

INTRODUCTION

Monitoring the distribution of water in the shallow subsurface, up to a few tens of meters, is crucial for addressing various geophysical, geotechnical, and geoenvironmental challenges, e.g., assessing the stability of dikes and slopes, monitoring the hydraulic processes at waste disposal sites, and managing agricultural irrigation. Geophysical approaches offer a cost-effective, in situ, and noninvasive solution for monitoring the shallow subsurface below relatively large areas. Robinson et al. (2008) discuss geophysical instrumentation, measurements, and modeling, especially pertaining to electrical and magnetic methods that are useful for watershed-scale hydrology. There have been attempts to invert electrical and electromagnetic (EM) measurements to obtain the hydrologic parameters (e.g., Hercknrath, 2012). A recent review by Whiteley et al. (2018) highlights the advantage of geophysical methods in monitoring landslides related to near-surface water distribution. Although electrical and EM methods are commonly used to investigate near-surface water distribution, seismic methods are valuable for identifying water table (WT) fluctuations and the related structural weaknesses, e.g., for geotechnical remediation of levees (e.g., Lorenzo et al., 2014).

Because the velocity of S waves (V_S) in soft soils is generally significantly smaller than the velocity of P waves (V_P), with the V_P/V_S ratio often exceeding 5–7, for similar frequencies, the wavelength of S waves is much shorter than that of P waves. This results in much higher resolution using S waves, in case of soft soils. Such high-resolution potential of S waves to image the shallow subsoil has been known for a long time (e.g., Deidda and Balia, 2001; Ghose and Goudswaard, 2004). In addition, changes in V_S due to variations in water content would reflect changes in density and effective stress.

Manuscript received by the Editor 28 September 2024; revised manuscript received 13 December 2024; published ahead of production 12 January 2025; published online 2 April 2025.
[1]National Institute of Advanced Industrial Science and Technology, Geological Survey of Japan, Tsukuba, Japan. E-mail: s.minato@aist.go.jp (corresponding author).
[2]Delft University of Technology, Department of Geoscience and Engineering, Delft, the Netherlands. E-mail: r.ghose@tudelft.nl.

The shallow subsurface typically consists of unconsolidated soils with low confining stresses (generally in the range of hundreds of kPa at depths of tens of meters). As a result, changes in the effective stress due to variations in pore pressure or suction can have a significant impact on V_S. The relationship between V_S and water content in such near-surface environments has been a topic of extensive theoretical and experimental research. For example, V_S in unconsolidated soils has been measured in laboratory settings under saturated and unsaturated conditions to explore its relationship with the applied stress (e.g., Velea et al., 2000; Cho and Santamarina, 2001; Zimmer et al., 2007; Sawangsuriya et al., 2009; Ghose, 2010; Whalley et al., 2011, 2012). Empirical relationships and theoretical models have also been proposed to describe how V_S is influenced by stress and water content (e.g., Santamarina and Cascante, 1996; Dvorkin et al., 1999; Avseth et al., 2010; Shen et al., 2016; Romero-Ruiz et al., 2021; Solazzi et al., 2021). Field experiments have primarily used V_S to estimate saturated areas based on the V_P/V_S ratio (Williams et al., 2003; Liberty and Gribler, 2014; Lorenzo et al., 2014; Pasquet et al., 2015; Konstantaki et al., 2016). In addition, near-surface V_S measurements for monitoring fluid at depths from a few meters to tens of meters have been reported in many previous studies (e.g., West and Menke, 2000; Konishi et al., 2015; Bergamo et al., 2016; Whiteley et al., 2020; Qin et al., 2022).

Conventionally, monitoring of near-surface V_S has relied on surface-wave analyses, primarily due to the cost considerations. Only a few examples of near-surface monitoring using body S waves have been presented to date. For example, Whiteley et al. (2020) explore the utility of body S-wave tomography for landslide monitoring, whereas Locci-Lopez and Lorenzo (2023) attempt to estimate pore pressure changes in levees based on the stacking velocity of reflected S waves. However, the capability of S-wave measurements to delineate in high-resolution the changes in soils due to changing water conditions remains still poorly understood. Furthermore, the extent to which the field-observed changes in V_S can be quantitatively attributed to the changes in the water condition is still unclear. This is partly due to the mixed effects of natural moisture changes, such as rainfall and fluctuating water levels, and the uncertainties related to subsurface heterogeneity.

In this study, we conducted a body S-wave tomography experiment on a field-scale test dike with controlled water levels, to investigate the impact of changes in density and shear modulus on the observed V_S variations. This investigation approach permits isolating and examining the various effects of water-level-related changes in a known structure. By gradually raising the water level on one side of the dike, we were able to estimate with a high resolution which parts of the dike were affected. In what follows, we first briefly review the theoretical background of how V_S changes might be influenced by the presence of water, followed by presentation of results from the V_S monitoring on our test dike.

THEORY REVIEW: V_S AND PRESENCE OF WATER

V_S as a function of bulk density and stress

In this section, we specifically focus on the effect of water on V_S due to changes in bulk density (ρ_b) and effective stress (σ'). The term V_S is a function of ρ_b and shear modulus (G_0) such that

$$V_S = \sqrt{\frac{G_0}{\rho_b}}. \tag{1}$$

The ρ_b is a function of water saturation (S_W):

$$\rho_b = (1-\phi)\rho_g + S_W\phi\rho_w, \tag{2}$$

where ϕ is porosity, ρ_g is the density of the grain, ρ_w is the density of water, and the density of air is assumed to be zero. The small-strain shear modulus G_0 can be expressed as a function of σ' as

$$G_0 = A\sigma'^B, \tag{3}$$

where A and B are coefficients. Numerous theoretical and experimental studies support this form of the equation. In classical contact theory (e.g., Hertz-Mindlin theory), the coefficient A is a function of parameters describing microstructures and mechanical properties of the material, whereas B is typically 1/3. Primarily based on laboratory experiments, geotechnical engineers were first to propose various expressions relating the coefficient A to void ratio or porosity (e.g., Hardin and Black, 1966; Ishihara, 1982; Stokoe et al., 1985; Saxena et al., 1988; Jamiolkowski and Lo Presti, 1994). This form (equation 3) for G_0 was suggested for unconsolidated fully saturated soils (e.g., Bachrach et al., 1998; Dvorkin et al., 1999; Ghose, 2010) and for partially saturated soils (e.g., Cho and Santamarina, 2001; Shen et al., 2016; Romero-Ruiz et al., 2021; Solazzi et al., 2021). Subsequently, empirical relationships for G_0 or V_S were found to follow the same form (e.g., Santamarina and Cascante, 1996; Zimmer et al., 2007; Sawangsuriya et al., 2009), with A and B as fitting parameters related to soil properties, such as void ratio and overconsolidation ratio.

We examine changes in V_S using equations 1–3 and the Hertz-Mindlin contact theory, as outlined by Solazzi et al. (2021). It is important to note that the contact theory is often coupled with Gassmann's fluid substitution equation to account for the presence of water (e.g., Bachrach et al., 1998; Dvorkin et al., 1999; Shen et al., 2016; Solazzi et al., 2021). In Gassmann's equation, the matrix shear modulus is assumed to remain unchanged between dry and wet conditions, meaning that the effect of saturation on G_0 is considered solely through changes in σ'. In this context, we have

$$A = \frac{2+3f-(1+3f)\nu}{5(2-\nu)}\left(\frac{3n^2(1-\phi)^2G^2}{2\pi^2(1-\nu)^2}\right)^{\frac{1}{3}}, \tag{4}$$

$$B = \frac{1}{3}, \tag{5}$$

$$\sigma' = \sigma_c - \frac{S_W - S_{wr}}{1-S_{wr}}u_W, \tag{6}$$

where G and ν are the shear modulus and the Poisson's ratio for the grain, respectively, n is the average number of contacts per particle in a spherical packing, f is the fraction of nonslipping particles, σ_c is the confining stress, S_{wr} is the residual water saturation, and u_W is the water pressure. In these equations, we assume the air pressure to be zero and the effective stress parameter (Bishop's parameter) controlling the contribution of water pressure to be equal to the effective saturation (Nuth and Laloui, 2008). Water pressure u_W is typically negative under unsaturated conditions ($S_W < 1$) due to suction and positive under saturated conditions ($S_W = 1$). When

direct measurement of σ_c is unavailable, it can be estimated from the overburden pressure. For example, under isotropic stress conditions, σ_c can be calculated from the ρ_b profile as $\sigma_c(z) = \int_0^z \rho_b(h) g dh$. For saturated conditions, equation 6 reduces to Terzaghi's effective stress, $\sigma' = \sigma_c - u_W$. For unsaturated conditions, u_W is a function of S_W, described by the soil-water characteristic curve (SWCC), which depends on the soil type (e.g., Assouline et al., 1998; Likos et al., 2014).

Numerical examples: Homogeneous soil column with changing water levels

To develop a procedure to evaluate the value of V_S affected by water, we perform calculations for a homogeneous soil column with the WT located at 1 m depth (Figure 1a–1f). Two different soil types are considered: "sand" and "clay." The necessary parameters for the SWCC (van Genuchten parameters), porosity, and grain properties for sand and clay are taken from the "Esperance sand" and the "Missouri clay" models, respectively, as presented in Solazzi et al. (2021). First, we calculate the saturation profile (Figure 1a) based on the WT depth and the water pressure profile (Figure 1b), assuming hydrostatic conditions (Solazzi et al., 2021). Under hydrostatic conditions, water pressure is independent of soil type (Figure 1b). Below the WT, the soil is fully saturated ($S_W = 1$), whereas above the WT, the saturation varies with depth (partially saturated condition). The differences in the saturation profiles for sand and clay (the red and black lines in Figure 1a) are due to their differing SWCC properties; clay retains more saturation than sand for the same water pressure. This results in higher saturation values in the unsaturated zone for clay. In contrast, the saturation in sand decreases sharply to the residual saturation (S_{wr}) just above the WT (see red line in Figure 1a). Using this saturation profile, we calculate the ρ_b profile (Figure 1c) through equation 2. This ρ_b profile is essential for determining the confining pressure, which then provides σ' (Figure 1d) via equation 6. The σ' profile is used to calculate G_0 (Figure 1e) through equation 3. Finally, we compute the V_S (Figure 1f) from G_0 and ρ_b using equation 1. Due to changes in saturation regime, the V_S exhibits a discontinuity at 1 m depth (Figure 1f), which is more pronounced for sand than for clay, primarily due to the sharp change in ρ_b in sand.

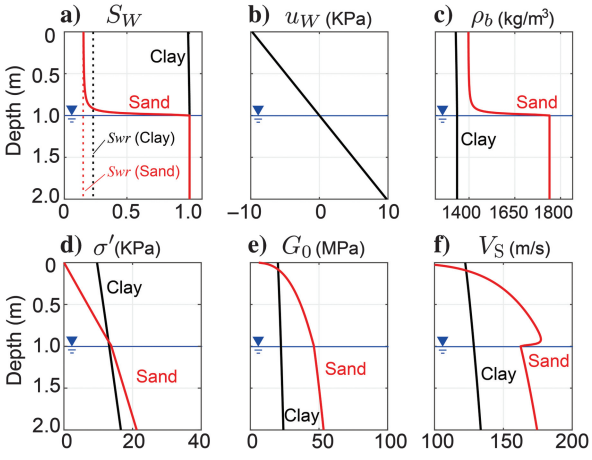

Figure 1. Numerical illustrations for a homogeneous soil column. (a) Saturation profile, (b) water pressure profile, (c) bulk density profile, (d) effective stress profile, (e) shear-modulus profile, and (f) S-wave velocity profile.

Next, we focus on the changes in ρ_b, G_0, and V_S at 1 m depth, when the WT depth is variable (Figure 2a–2c). When the WT is between 0 and 1 m depth, the 1 m depth level is fully saturated. Under these conditions, ρ_b remains constant (see the "saturated" area in Figure 2a), and changes in V_S are driven by variations in G_0 due to σ' ("saturated" area in Figure 2b and 2c).

When the WT is between 1 and 2 m depth, the 1 m depth level is partially saturated, and ρ_b and G_0 affect V_S. In the sand model, a significant velocity change occurs around the 1 m WT (the red line in Figure 2c), primarily due to a sharp change in ρ_b (the red line in Figure 2a). In contrast, for the clay model, changes in V_S with the WT are primarily due to variations in G_0 (the black line in Figure 2b). This result highlights the importance of ρ_b, G_0, and soil type to evaluate the changes in V_S at a specific depth due to fluctuations in the WT.

DESCRIPTION OF THE EXPERIMENT

A test dike

We performed the experiments on a test dike located in Delft, the Netherlands. The dike was developed as part of the Flood Proof Holland project for a piping experiment (Pol et al., 2021). It has a maximum height of 1.8 m, a minimum base length of 10 m,

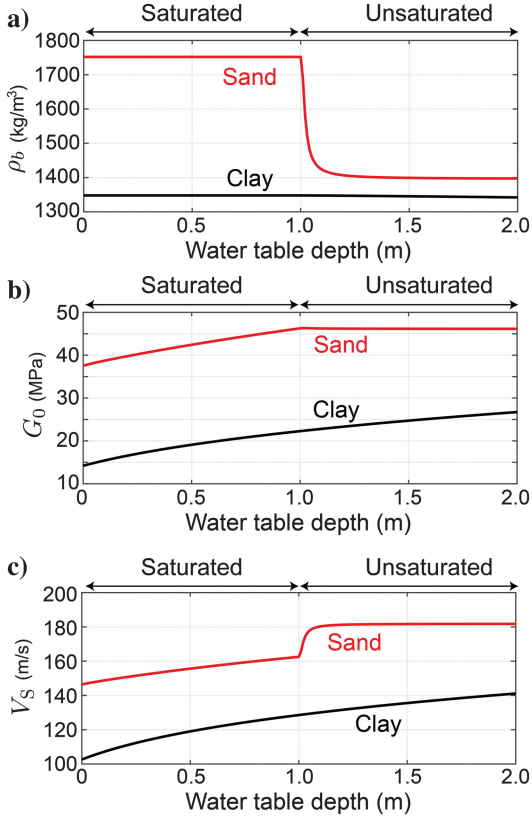

Figure 2. At 1 m depth, the changes in (a) bulk density (ρ_b), (b) shear modulus (G_0), and (c) S-wave velocity (V_S) when the depth of the WT varies. The sharp contrast at WT depth of 1 m is due to the transition from saturated conditions (when the WT is between 0 and 1 m) to unsaturated conditions (when the WT is below 1 m).

and an approximate length of 15 m in the longitudinal direction (Figure 3a). The dike consists of a sand body covered by a clay layer on the slopes and at the crest (see the cross section in Figure 3b). On the high-water side, a water reservoir constructed with concrete slabs allows control of the water level on the slope. An additional clay layer at the base of the sand body hydraulically separates the dike body from an artificial aquifer below (Figure 3b). Furthermore, the entry pipes for water infiltration into the aquifer (Pol et al., 2021) were sealed during the measurements, allowing water from the reservoir to preferentially infiltrate into the dike body and exit at the low-water-side slope. More details on the construction of the test dike can be found in Pol et al. (2021).

Data acquisition

In this study, we perform first-arrival tomography on four time-lapse seismic data sets corresponding to four different water levels (Figure 4). Data were collected once a day over four consecutive days, with no recorded precipitation during the measurement campaign. On day 1, the measurements were taken under initial conditions, with no water in the reservoir. Twenty-one sources at 50 cm interval and 42 receivers at 25 cm interval were installed along the dike. We used an SH (shear-horizontal) portable vibrator (Ghose et al., 1996; Ghose, 2012) with a sweep frequency range of 30–450 Hz and horizontal component geophones as receivers. An auger was used to locate the WT in the dike but none was found under the initial conditions, at least until 1 m from the surface.

After the first day's measurement, we increased the water level on the high-water-side slope by filling the reservoir. The infilling was stopped when the water level reached 60 cm from the bottom of the slope. The dike was then left undisturbed for at least 12 h to allow water infiltration into the dike, before acquiring seismic data for tomography on day 2. By the time the data were collected, the water level on the slope had decreased to 49 cm due to infiltration, representing a significant decrease over the 12 h span. This corresponds to approximately 20% of the initial water volume infiltrating into the dike, calculated using the size of the water reservoir as presented in Yagisawa et al. (2019) and the average slope angle of our survey line (21°). The receiver positions remained the same as on day 1 but the number of sources was reduced on day 2 because part of the slope became inaccessible due to the rising water (see Figure 4b). The water level was detected through augering at two locations within the dike (the blue dots in Figure 4b). The WT where the pore pressure equals atmospheric pressure (the dashed blue line in Figure 4b) was calculated through numerical modeling, assuming a stationary flow (see Appendix A). This procedure was repeated with water levels increased to 1 m for day 3 (Figure 4c) and to 1.5 m for day 4 (Figure 4d). The water levels on the slope immediately before measurements were 92 cm on day 3 and 125 cm on day 4. Importantly, during the approximately 1.5 h data acquisition periods on each day, the water level decreased by only a few centimeters. Thus, we assume that during these relatively short measurement windows, any changes in the water distribution are negligible.

Figure 5 shows an example of the measured data at various water levels. Data from a source located near the crest on the high-water-side slope of the dike (see Figure 5a) are plotted here for different

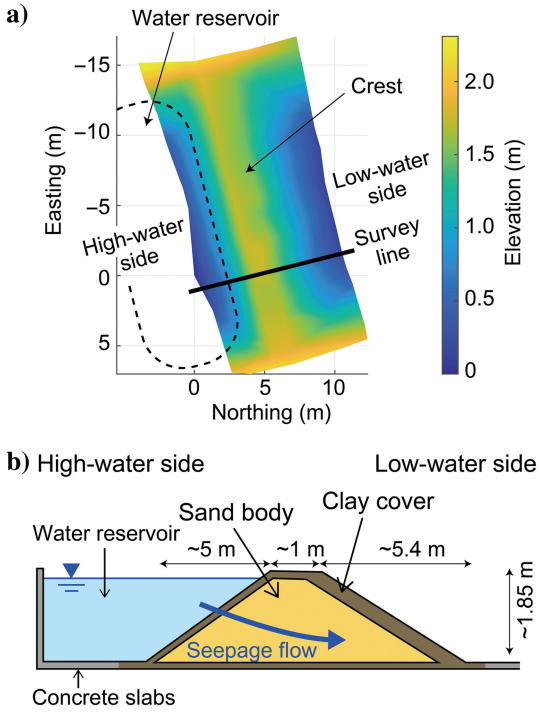

Figure 3. Test dike geometry. (a) The elevation map of the test dike from global navigation satellite system measurement and (b) the schematic cross section at the survey line.

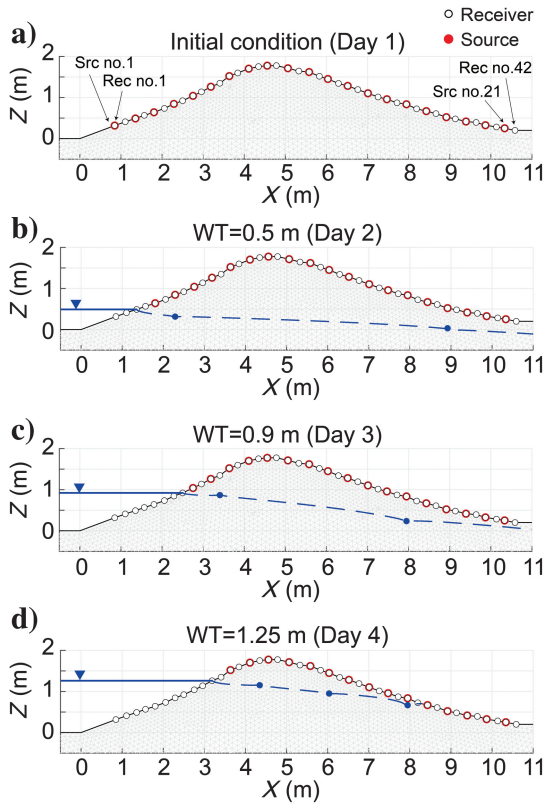

Figure 4. The source-receiver configuration (source = red circle, receiver = white circle) and the water levels at the slope as detected by auger (blue dots). (a) Initial condition (day 1), (b) WT on the high-water side slope at 0.5 m from the bottom of the slope (day 2), (c) WT at 0.9 m (day 3), and (d) WT at 1.25 m (day 4).

WT depths. The waveform data (Figure 5b), obtained after cross-correlation of the raw vibrograms with a reference signal, show clear first-arriving SH waves. Four shot gathers are stacked at each location. Careful forward modeling established that these first arrivals are of S waves traveling through the dike body and they are not surface waves. This will be illustrated subsequently in greater details while discussing the results. The measured waveforms remain coherent across different water levels data sets, indicating a high signal-to-noise ratio. The picked traveltimes (Figure 5c) show a noticeable increase as the water level rises, suggesting a velocity decrease due to water infiltration into the dike.

Inversion method

The picked traveltime data for all source-receiver pairs are used in first-arrival tomography. The tomography solves the following optimization problem using an iterative least-squares inversion:

$$E(\mathbf{m}) = \|f(\mathbf{m}) - \mathbf{d}\|_2^2 + \lambda\|\mathbf{L}\mathbf{m}\|_2^2 \rightarrow \min, \qquad (7)$$

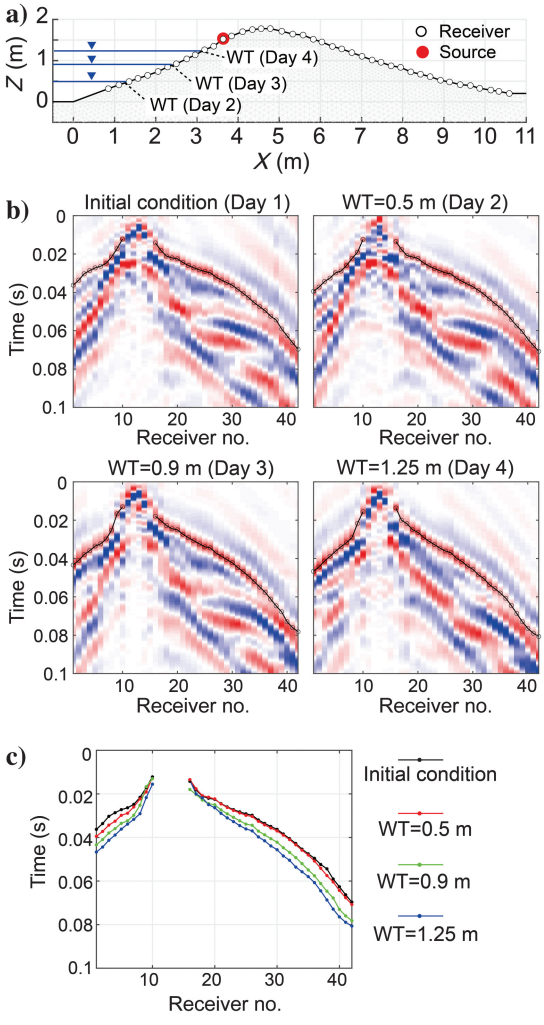

Figure 5. Data example at different water levels at the slope. (a) Source-receiver configuration and water levels, (b) waveform data at each water level, and (c) comparison of the picked first-arriving traveltimes in (b).

where $\mathbf{m}$ is the velocity model, $\mathbf{d}$ is the traveltime data, f is the forward-modeling operator, $\mathbf{L}$ is the operator that calculates the roughness of the model $\mathbf{m}$, and $\|\cdot\|_2^2$ represents the squared l^2 norm. The regularization parameter λ controls the balance between the model misfit (the first term in equation 7) and the model roughness (the second term in equation 7).

We used the open-source code pyGIMLi (Rücker et al., 2017) to solve the optimization problem. The code uses Dijkstra's algorithm for forward modeling and the conjugate gradient least-squares method for updating the velocity model.

RESULTS

First-arrival tomography

We performed tomographic inversion on four data sets corresponding to four different water levels. The initial model for the inversion was the same for all data sets, with the velocity linearly increasing with depth from the surface (Figure 6). The regularization parameter λ was determined based on the discrepancy principle, using data errors estimated from the L-curve analysis (Appendix B). The traveltimes for all source-receiver pairs were inverted and compared with those calculated using the tomographic V_S model (Figure 7). As explained previously, a part of the source locations was missing when the water levels were high (Figure 7). The estimated traveltimes accurately represent the observed data, as confirmed by the final data-misfit distribution (the difference between the observed and modeled traveltimes, Figure 8). The errors followed a Gaussian distribution estimated using the L-curve (Figure B-1) and also as assumed in the inversion, indicating that the inversion was successfully performed.

The inverted tomography models are shown in Figure 9. Due to variations in source locations, the ray coverage differs at different water levels (the area with low ray coverage is shown as a gray-shaded region in Figure 9). Some data (shot gathers) show a clear reflection signal at the zero-offset trace (e.g., Figure 5b) at approximately 0.025 s, which we interpret as that originating from the boundary between the clay cover and the sand body. These reflections are converted to depth using the tomographic velocity models (the white dots in Figure 9). The interpreted boundary between the clay cover and the sand body (the dashed white line in Figure 9) is based on these reflection depths, the inverted velocity structure, and the known geometries from the previous studies (Pol et al., 2021).

Under the initial condition (day 1), the clay cover has a V_S of approximately 60 m/s, and the sand body a V_S of 160 m/s (Figure 9a). When the water level on the slope increases to 0.5 m (day 2), the V_S on the high-water side slightly decreases (Figure 9b). As the water level further rises (day 3–day 4), the V_S throughout the entire structure decreases (Figure 9c and 9d). The reflection depth remains stable throughout the measurements (white dots in Figure 9).

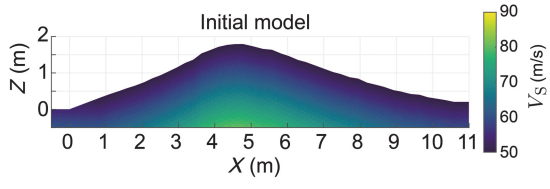

Figure 6. Initial model for the tomographic inversion.

Time-lapse V_S changes

The V_S changes from the initial condition to those corresponding to different water levels are shown in Figure 10. As previously discussed, the V_S begins to decrease on the high-water side by day 2 (Figure 10a), with a negligible change occurring on the low-water side. However, from day 3, the V_S decreases across the entire dike (Figure 10b), and at the highest water level (Figure 10c), the maximum V_S decrease reaches approximately 60 m/s, corresponding to a reduction of approximately 30% of the initial velocity. The V_S change is more pronounced in the sand body than in the clay cover. Note that a slight velocity increase at approximately $X = 8$–8.5 m in Figure 10b is likely an artifact caused by the acquisition footprint near the source at a very shallow depth.

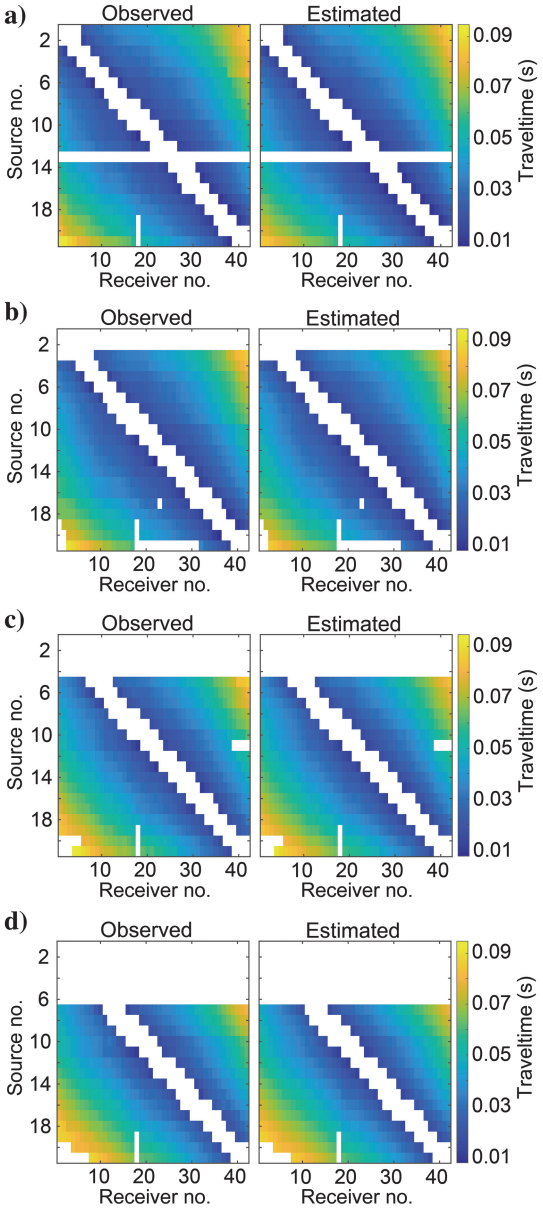

Figure 7. Observed and estimated traveltimes from the inversion. (a) Initial condition (day 1), (b) WT at 0.5 m (day 2), (c) WT at 0.9 m (day 3), and (d) WT at 1.25 m (day 4).

DISCUSSION

Effect of ρ_b and G_0 in time-lapse change of V_S

We observed the change in V_S at different water levels (Figure 10). As shown in equation 1, V_S is a function of ρ_b and G_0. In our experiment, it can be interpreted that the initially unsaturated zone becomes fully saturated during water infiltration, particularly on the high-water-side slope. In this zone, the observed V_S change reflects a combined effect of changes in ρ_b and G_0.

Previous studies have discussed the correlation between V_S changes and variations in the WT and/or in the precipitation history (e.g., West and Menke, 2000; Qin et al., 2022), concluding that the V_S changes are primarily due to water, particularly in the fully saturated zones. In such cases, changes in ρ_b are negligible, and the V_S change is primarily attributed to variations in the G_0. However, limited research has addressed the extent to which field data reflect changes in ρ_b and G_0.

To discuss the interplay between ρ_b and G_0, we evaluate the squared velocity ratio:

$$\left(\frac{V_S^{\text{Day3}}}{V_S^{\text{Day1}}}\right)^2 = \frac{\rho^{\text{Day1}}}{\rho^{\text{Day3}}} \times \frac{G_0^{\text{Day3}}}{G_0^{\text{Day1}}}. \tag{8}$$

This ratio represents the product of changes in ρ_b and G_0 from day 1 (initial conditions) to day 3 (with the water level at 0.9 m). The ratio (Figure 11a) shows values smaller than one throughout most of the

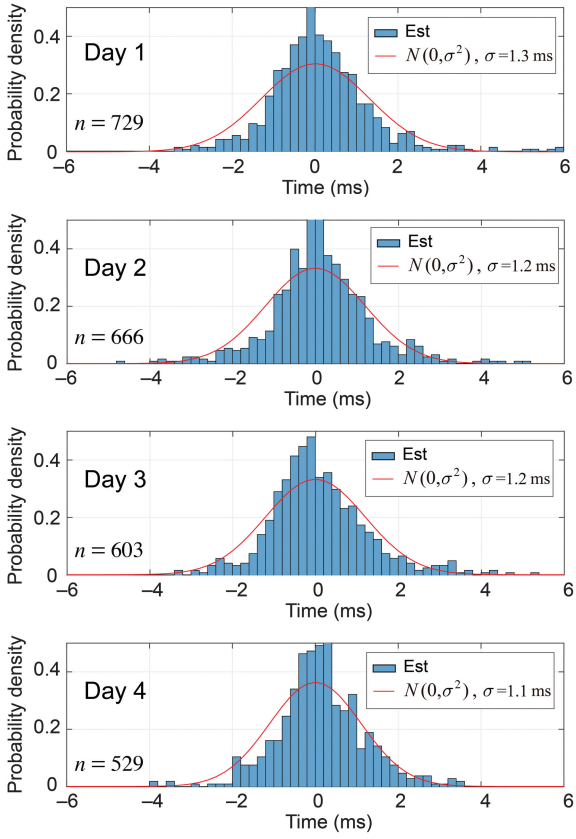

Figure 8. Final data-misfit distribution (blue box) and the distribution assumed in the inversion (red line) for each data set.

model, indicating a velocity decrease across the entire dike. A vertical slice of the ratio at the $X = 3.41$ m, where the WT was detected on day 3 (the solid black line in Figure 11a), is shown in Figure 11b. We assume that the area below the detected WT on day 3 was initially unsaturated but became fully saturated due to water infiltration. This zone shows the squared velocity ratio between 0.65 and 0.80 (see solid red line in the right figure in Figure 11b), which is mostly in the sand body. Note that in Figure 11b, the WT is plotted lower than 0.9 m (the dashed blue line), reflecting that the internal WT within the dike goes down toward the low-water-side slope.

We estimate the possible change in ρ_b within this zone. Using the definition of ρ_b (equation 2), we calculate the range of its values. The porosity of the sand in the field is assumed to be 0.38, based on the laboratory measurements on soil samples collected from the field (Pol et al., 2021). The grain density (ρ_g) and water density (ρ_w) are assumed to be 2650 and 1000 kg/m^3, respectively. On day 3, we assume full water saturation, while the initial water saturation is unknown. To estimate the possible maximum change in ρ_b, we consider initial water saturation (S_W) ranging from 0 to 0.5. This gives a calculated ρ_b change (as a ratio) between 0.8 and 0.9, suggesting that the change in G_0 is not negligible. The range of G_0 change (as a ratio) is estimated to be between 0.7 and 1.0.

Effect of stress in time-lapse change of V_S

In the previous subsection, we discussed that the changes in G_0 likely contribute to the observed changes in V_S. As shown in equation 3, G_0 changes due to changes in σ'. In this subsection, we explore the extent to which the observed V_S changes can be explained by changes in σ'.

We use the same V_S ratio as in equation 8 but this time we compare the data from day 3 (water level at 0.9 m) and day 4 (water level at 1.25 m) because the saturation area is large, and there is a significant water-level change within the area imaged by tomography in these data sets. The values at $X = 3.41$ m and $X = 7.95$ m are analyzed to assess the effect of σ' (Figure 12). The black arrows

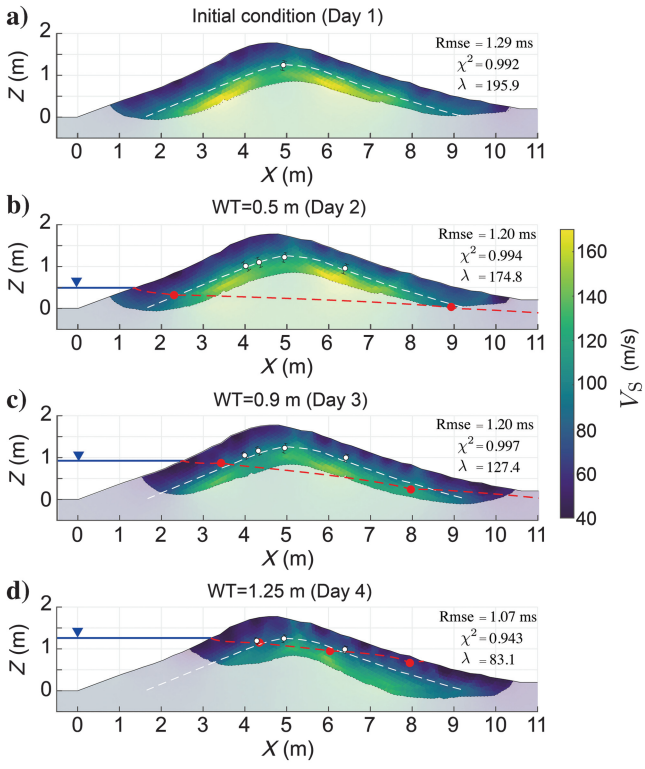

Figure 9. Inverted V_S models. (a) Initial condition (day 1), (b) WT at 0.5 m (day 2), (c) WT at 0.9 m (day 3), and (d) WT at 1.25 m (day 4). The dashed white line is the interpreted clay-sand boundary. The white dots indicate the location of the clay-sand boundary from the reflection signal (see the main text).

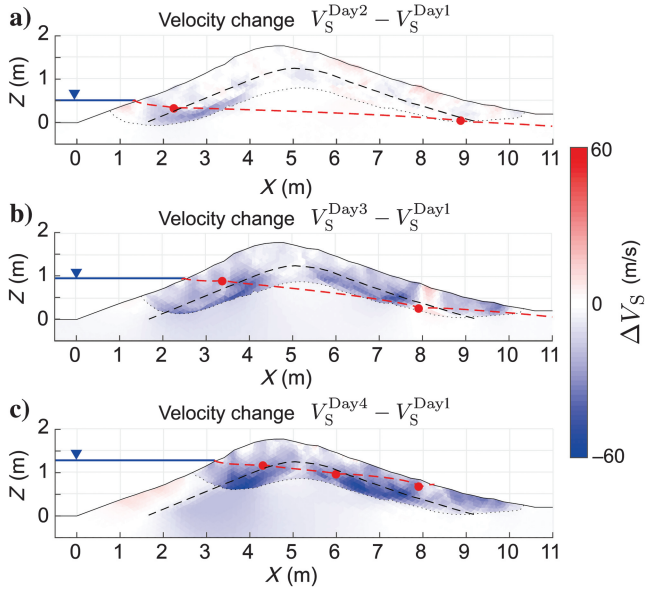

Figure 10. Estimated velocity change from the initial condition to conditions corresponding to different water levels. (a) WT at 0.5 m (day 2), (b) WT at 0.9 m (day 3), and (c) WT at 1.25 m (day 4).

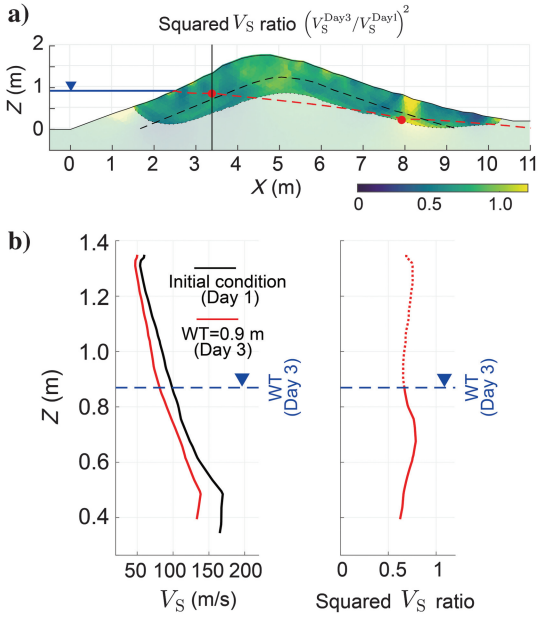

Figure 11. (a) Squared V_S ratio for the initial condition (day 1) and when WT is at 0.9 m (day 3) and (b) values at $X = 3.41$ m (solid black line in [a]).

in Figure 12b and 12c show the zones which remained saturated throughout the measurements. In these zones, the V_S ratio reflects only the change in G_0:

$$\left(\frac{V_S^{\text{Day4}}}{V_S^{\text{Day3}}}\right)^2 = \frac{G_0^{\text{Day4}}}{G_0^{\text{Day3}}} = \left(\frac{\sigma'^{\text{Day4}}}{\sigma'^{\text{Day3}}}\right)^B, \quad (9)$$

where we use equation 3. From the squared V_S ratio, we can estimate the change in σ', assuming B is constant at each depth during the measurement. The gray hatched areas in Figure 12b and 12c show the estimated σ' ratio, assuming B values range from 1/3 to 2/3, a typical range reported in literature (Zimmer et al., 2007). The estimated stress ratio ranges from 0.25 to 0.64 at X = 3.41 m, and from 0.33 to 0.90 at X = 7.95 m. At the low-water-side slope (X = 7.95 m), the estimated σ' ratio covers the ratio calculated from the numerical modeling, which takes into consideration the dike topography and the detected water levels under the assumption of a stationary flow (the solid black line in Figure 12c and Appendix A). However, at the high-water-side slope (X = 3.41 m), the estimated σ' ratio is significantly smaller (indicating a larger change) than the numerical modeling prediction (the solid black line in Figure 12b). One possible explanation for the larger change in σ' observed in the field is the presence of excess pore pressure. Because our experiment did not control the flow conditions, the seismic measurements probably have been conducted under dynamic flow conditions, where localized pore pressure exceeded those expected under the stationary flow. Note that the deviations between the field data and the numerical modeling might be due to limitations in resolution and accuracy at the high-water-side slope owing to limited ray coverage. Synthetic modeling that simulates the missing source locations using the tomographic model could help clarify this discrepancy better.

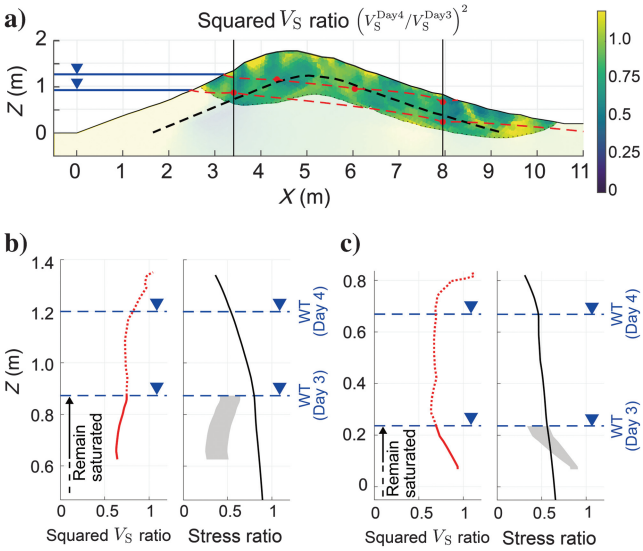

Figure 12. (a) Squared V_S ratio estimated from field data for WT at 0.9 m (day 3) and WT at 1.25 m (day 4). (b) The V_S ratio at X = 3.41 m (red line), the range of σ' ratio (gray hatch) estimated from the V_S ratio (equation 9) in the fully saturated zone, and the σ' ratio (solid black line) calculated from the numerical modeling (see Figure A-2). See the main text for more details. (c) Same as (b) but at X = 7.95 m.

Verification of tomographic velocity model using synthetic waveforms

To verify the tomographic velocity model (Figure 9), we calculate synthetic waveforms using the model derived for the initial condition (day 1, Figure 13a). We use the 2D SH wavefield modeling using the finite-difference time-domain method (Köhn et al., 2012), discretizing the velocity model with a 0.01 m grid spacing. The free-surface boundary condition is approximated using the vacuum method (e.g., Graves, 1996). A source wavelet is extracted from the field data (near-offset records in Figure 5b) by time windowing and then averaging the waveforms. Because 2D wavefield modeling assumes a line source, the synthetic waveforms exhibit phase rotation compared with the 3D wavefield. We compensate for this rotation after calculating the wavefield, allowing the use of traveltimes at the peak amplitudes of the first-arriving waves as our traveltime data.

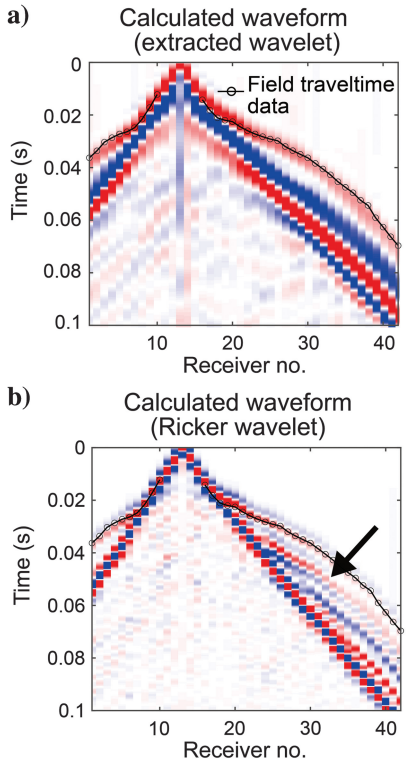

Figure 13. Synthetic waveforms using the tomographic V_S model (Figure 9a). (a) The result using the wavelet extracted from the field data. The source-receiver configuration is same as in Figure 5a. The black circles show the picked traveltimes in the field data. (b) Same as (a) but using the wide bandwidth wavelet. The black arrow indicates the multiple reflections from the clay-sand boundary.

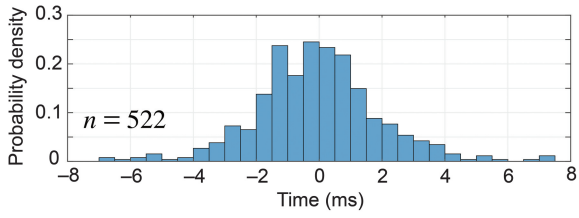

Figure 14. Distribution of the reciprocal traveltime error.

The peak amplitudes of first arrivals correspond well to the picked traveltimes from the field data (the black lines in Figure 13a). Moreover, the observed and synthetic waveforms are notably similar, especially around the first arrivals (compare "Initial condition (day 1)" in Figures 5b and 13a). The large-amplitude event after the first-arriving wave is identified as Love waves. To further discuss wave modes, we recalculate the waveform using the same source-receiver configuration but with a wide-bandwidth wavelet (Figure 13b). For this, we use a Ricker wavelet with a center frequency of 150 Hz. The modeled data and the snapshots confirm that, shortly after the first-arriving body waves, multiple reflections from the clay-sand boundary arrive (the black arrow in Figure 13b). These reflections possibly interfere with the first-arriving body waves, depending on the shape and frequency content of the source wavelet. However, the interference is not significant in our modeling example which uses the wavelet extracted from the field data (Figure 13a).

Finally, some differences are observed between the modeled and the observed Love waves and the later arrivals (e.g., 0.06 s and later at the receiver number 20–40 in Figures 5b and 13a). The complex wave events following the first arrivals in the observed data are likely off-plane scatterings due to buried objects, such as entry pipes, or the edge of the test dike in the longitudinal direction (see Figure 3a). These results suggest that near-surface seismic waveform inversion (see Pan et al. [2019] and references therein) could be applied to improve the accuracy and resolution of the V_S structure. However, to achieve this, it will be necessary to consider the 3D wavefield (e.g., Tran et al., 2019; Irnaka et al., 2022; Kawasaki et al., 2024).

Uncertainty in the estimated velocity and the data error

In this study, we assumed the data error based on the L-curve analysis (Appendix B). To provide an independent assessment, we also estimate the data error using reciprocal traveltime (Whiteley et al., 2020). The reciprocal traveltime error is defined as the difference of the picked traveltime of the reciprocal measurements, where the source and receiver locations are swapped. Across all data sets, 522 such measurements are identified, showing a Gaussian distribution with a standard deviation of 2.0 ms (Figure 14). Note that this error is larger than the value assumed in the inversion (Figure 9), derived from the L-curve (Appendix B).

When the reciprocal traveltime error of 2.0 ms is used in the inversion, smooth V_S models are obtained (Figure 15). This is because the discrepancy principle imposes large smoothness constraints for large data errors to avoid overfitting data. In this case, the estimated V_S range (Figure 16a) and the temporal V_S change at day 4 relative to the initial condition (Figure 16b) are smaller than those obtained with smaller assumed errors. Specifically, with a data error of 2.0 ms, the maximum V_S decrease is approximately 40 m/s, corresponding to approximately 25% of the initial velocity.

It is important to note that the corner of the L-curves is not observed at approximately 2.0 ms (see the figure in Appendix B). Because the reciprocal traveltime error is derived from a subset of the data (522 measurements out of a total of 2527), whereas the L-curve analysis uses the entire data set, this error might be overestimated. However, the data-error estimation from the L-curve involved subjective interpretation. The short-wavelength V_S changes found in the results (Figure 10) suggest that underestimating the errors might introduce artifacts due to overfitting. Therefore, the results obtained using the reciprocal traveltime error (Figure 15) can be regarded as the most conservative representation.

Despite the uncertainty in the estimated V_S and the value of V_S changes, trends of the temporal changes of V_S remain consistent; a progressive velocity decrease originating in the high-water-side slope is observed across all scenarios (Figures 10 and 15). This consistent observation suggests that this feature is quite likely to be true, and that V_S monitoring successfully captures this feature in spite of uncertainties and possible data errors.

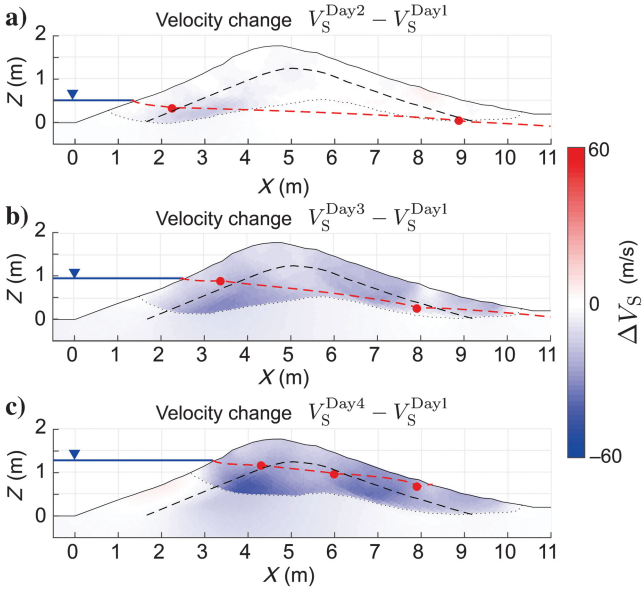

Figure 15. Estimated velocity change assuming the data error derived from the reciprocal traveltimes. (a) WT at 0.5 m (day 2), (b) WT at 0.9 m (day 3), and (c) WT at 1.25 m (day 4).

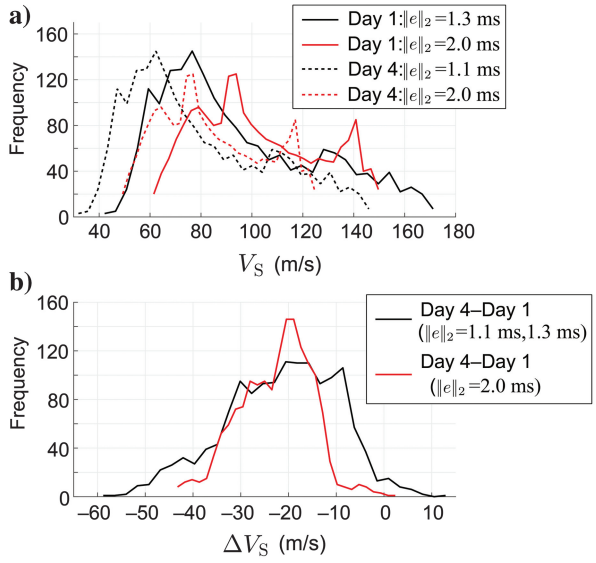

Figure 16. Distribution of (a) the estimated V_S and (b) the change of V_S between day 1 and day 4 under different assumed data errors.

Time-lapse V_S monitoring: Implications and opportunities

We demonstrated that first-arrival S-wave tomography could successfully capture the spatial changes in V_S induced by water infiltration in a field-scale test dike. Conventional near-surface geophysical methods often rely on surface wave analyses (e.g., multichannel analysis of surface waves) to estimate V_S. These methods offer notable practical advantages, including efficient data acquisition without the need for polarized sources or receivers and correlation-based phase velocity estimations that are less sensitive to time-zero shift or trigger delay. However, surface-wave analyses rely on a 1D layered earth model, which limits its spatial resolution in 2D profiling. This limitation may partially explain why relatively few studies have investigated shallow V_S changes using surface waves (e.g., Konishi et al., 2015; Bergamo et al., 2016).

We also explored the relationship between the observed V_S changes and the stress variations, finding partial consistency with the theoretical model (see subsection "Effect of stress in time-lapse change of V_S"). These results highlight the potential of V_S monitoring as a tool for stress monitoring, as previously suggested (Ghose, 2010). Such an approach could be particularly valuable for safety analyses of soil slopes, where stress distribution and temporal changes are often estimated through numerical modeling (e.g., Ng and Shi, 1998) rather than via data-driven analyses based on in situ measurements in the field. Moreover, the sensitivity of V_S to stress could be exploited in combination with other measurements, such as ERT for water content estimation, to derive SWCC directly in the field (e.g., Suzaki et al., 2017, 2018). Last but not the least, the differing responses of V_S to water content across various soil types (see subsection "Numerical examples: Homogeneous soil column with changing water levels") offer a potential for soil classification using time-lapse V_S changes, which otherwise involves invasive measurements.

CONCLUSION

We performed time-lapse S-wave tomography using data sets acquired on a test dike under varying water levels to monitor changes in the V_S structure. The results indicate that V_S decreases initially on the high-water-side slope when the water level is low, and this reduction extends across the entire dike as the water level rises. The V_S reduction is more pronounced in the sand body than in the clay cover, with a maximum decrease of approximately 40–60 m/s, corresponding to approximately 25%–30% reduction from the initial condition.

To understand the interplay between ρ_b and G_0 in the V_S changes observed within the unsaturated zone, we calculated the squared velocity ratio. The results suggest that ρ_b and G_0 greatly contribute to the observed changes in V_S. In the fully saturated zone, we used the squared velocity ratio to evaluate changes in σ'. Although the estimated stress changes on the low-water-side slope align well with the numerical modeling predictions, the high-water-side slope exhibits larger changes, likely due to the impact of the excess pore pressure.

ACKNOWLEDGMENTS

We sincerely thank OYO Corporation, Japan, for their support of this study and A. Suzaki for his assistance during the field survey. Our gratitude also extends to J. Pol for allowing us to use the Flood Proof Holland facility in Delft.

DATA AND MATERIALS AVAILABILITY

Data associated with this research are available and can be obtained by contacting the corresponding author.

APPENDIX A

SEEPAGE ANALYSIS

To estimate the possible water pressure distribution in the test dike, we perform seepage analysis using the known WTs at each measurement day. The analysis is achieved by evaluating 2D Richards equation (Richards, 1931; Lam et al., 1987):

$$\frac{\partial}{\partial x}\left(K\frac{\partial h}{\partial x}\right)+\frac{\partial}{\partial z}\left(K\frac{\partial h}{\partial z}\right)=\frac{\partial \theta}{\partial t}, \tag{A-1}$$

where x and z are spatial coordinates, t is time, K is the unsaturated hydraulic conductivity, h is the total hydraulic head, and θ is the volumetric water content. Note that K is calculated from the saturated and relative conductivity as a function of SWCC (Van Genuchten, 1980). We assume the topography of the test dike and the internal clay-sand structure (Figure A-1a) based

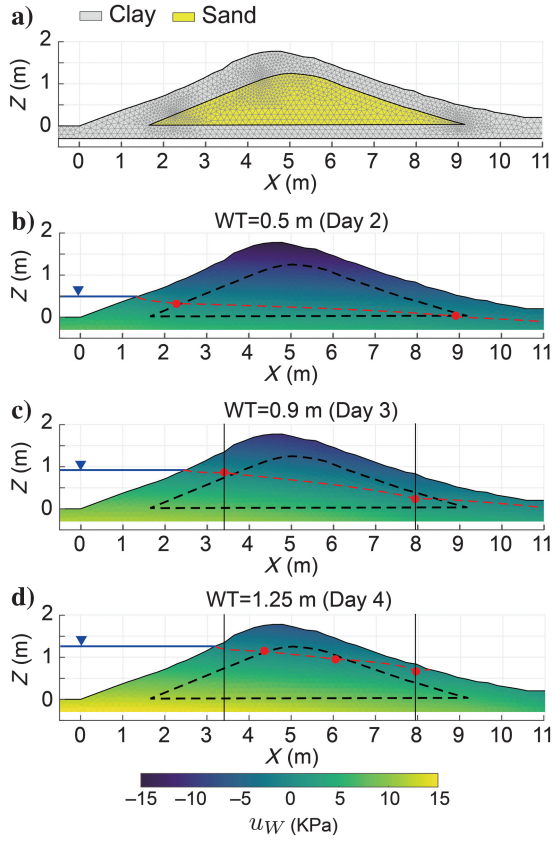

Figure A-1. Result of the seepage analysis. (a) Assumed structure and mesh geometry for the flow simulation and (b) water pressure distribution on day 2. WT on the high-water side (blue line) and water levels in the dike (red dots and dashed red line) are shown. (c and d) Same as (b) but on day 3 and day 4, respectively.

on prior knowledge (Pol et al., 2021). For boundary conditions, a fixed hydraulic head is assumed at the high-water-side slope using the water level (the blue lines in Figures A-1b–A-1d), zero water pressure is assumed at the edge of the low-water side at $(x, z) = (13, -0.3)$, and a fixed head is inside of the dike, where the presence of water is detected in the field (the red dots in Figures A-1b–A-1d). The rest of the model boundaries are assumed impermeable. We obtain the results of water pressure distribution (Figures A-1b–A-1d) with stationary flow conditions by evaluating equation A-1 with time (t) until the distribution of hydraulic head does not change (stationary). We use COMSOL Multiphysics software for the modeling. See Table A-1 for the assumed parameters in the seepage analysis.

After calculating the water pressure distribution, we calculate σ' at $X = 3.14$ m and $X = 7.95$ m for day 3 and day 4 (Figure A-2). For this purpose, we assume the grain density to be 2600 kg/m^3, porosity of clay 0.4, and that of sand 0.38. One can see that the change in σ' is driven more by the change of water pressure than that of confining stress (Figure A-2). The ratio in σ' between the day 3 and day 4 is calculated; this is shown in Figure 12b and 12c (the solid black lines).

Table A-1. Material parameters used for seepage analysis.

	Clay	Sand
Saturated water volume fraction	0.4	0.38
Residual water volume fraction	0	0
Saturated hydraulic conductivity	2.5e-5 (m/s)	9e-5 (m/s)
Van Genuchten parameters (α, n)	0.392 (1/m), 1.23	14 (1/m), 1.8

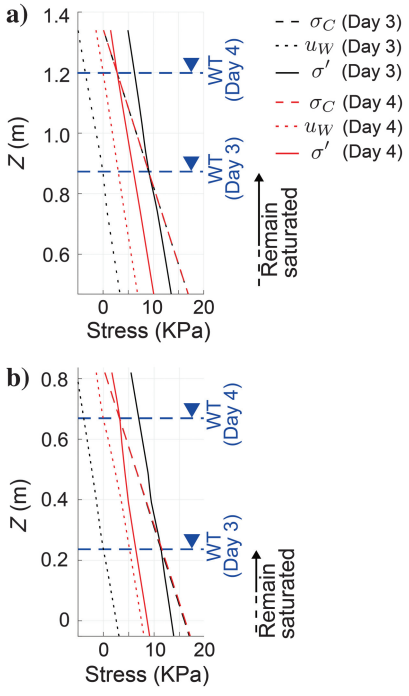

Figure A-2. (a) Calculated stress components at $X = 3.41$ m for day 3 and day 4 (see solid black line in Figures A-1c–A-1d) and (b) same as (a) but at $X = 7.95$ m.

APPENDIX B

REGULARIZATION PARAMETER

In tomographic inversion, it is important to select an appropriate value for the regularization parameter λ shown in equation 7. For this purpose, we use the discrepancy principle (Hansen, 2010). The idea of the discrepancy principle is to avoid overfitting the data by selecting the parameter λ such that the data misfit is as small as the error in the data, i.e., $f(\mathbf{m}) - \mathbf{d}_2 = e_2$. In this study, the data error e_2 is estimated from the L-curve (the plot of the residual norm versus solution norm with different value of λ, Figure B-1) because the corner of the L-curve is located roughly at the data error (Hansen, 2010).

We consider λ within a range from 1 to 10,000. When using the velocity model shown in Figure 6 as the initial model for each calculation, we observed that small values of λ produced a model with a large model roughness, causing the resulting L-curve to become unstable (the dotted blue line in Figure B-1). To circumvent this problem, we adopted a sequential approach: starting with the largest λ, we calculate the L-curve step by step, using the model estimated for the previous λ as the initial model for the next iteration. This approach produced a stable L-curve (the blue line in Figure B-1) with smaller misfit compared with using a fixed initial model. This improvement is likely due to the sequential approach which avoids entrapment in the local minima during the inversion process. The optimum value of λ is determined by interpolating the L-curve, based on an assumed value for the data error. The data error is visually estimated by identifying the corner of the L-curve. The assumed error for the data of the initial condition (day 1) is 1.3 ms, that for day 2 and day 3 is 1.2 ms, and that for day 4 is 1.1 ms (the dashed lines in Figure B-1). Considering that the data sampling interval is 1 ms, we believe that these errors are appropriate and can be assumed almost constant during the entire set of measurements. The tomographic V_S models shown in Figure 9 are inverted using the regularization parameter λ corresponding to the assumed errors.

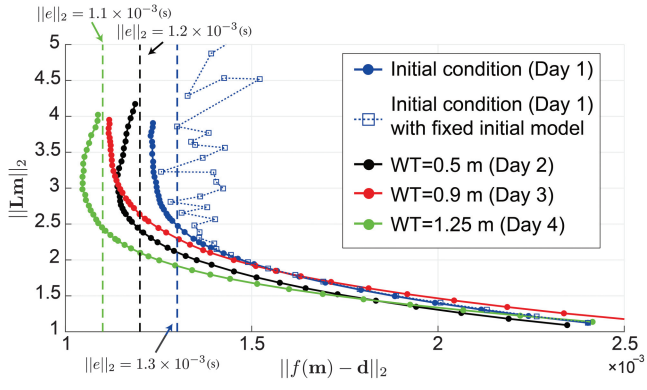

Figure B-1. L-curve plot with data misfit (horizontal axis) versus model roughness (vertical axis) for each data set. The dashed lines indicate the assumed data error (standard deviation) in the inversion.

REFERENCES

Assouline, S., D. Tessier, and A. Bruand, 1998, A conceptual model of the soil water retention curve: Water Resources Research, **34**, 223–231, doi: 10.1029/97WR03039.

Avseth, P., T. Mukerji, G. Mavko, and J. Dvorkin, 2010, Rock-physics diagnostics of depositional texture, diagenetic alterations, and reservoir heterogeneity in high-porosity siliciclastic sediments and rocks — A review of selected models and suggested work flows: Geophysics, **75**, no. 5, 75A31–75A47, doi: 10.1190/1.3483770.

Bachrach, R., J. Dvorkin, and A. Nur, 1998, High resolution shallow seismic experiments in sand, Part II: Velocities in shallow unconsolidated sand: Geophysics, **63**, 1234–1240, doi: 10.1190/1.1444424.

Bergamo, P., B. Dashwood, S. Uhlemann, R. Swift, J. E. Chambers, D. A. Gunn, and S. Donohue, 2016, Time-lapse monitoring of climate effects on earthworks using surface waves: Geophysics, **81**, no. 2, EN1–EN15, doi: 10.1190/geo2015-0275.1.

Cho, G. C., and J. C. Santamarina, 2001, Unsaturated particulate materials — Particle-level studies: Journal of Geotechnical and Geoenvironmental Engineering, **127**, 84–96, doi: 10.1061/(ASCE)1090-0241(2001)127:1(84).

Deidda, G. P., and R. Balia, 2001, An ultrashallow SH-wave seismic reflection experiment on a subsurface ground model: Geophysics, **66**, 1097–1104, doi: 10.1190/1.1487057.

Dvorkin, J., M. Prasad, A. Sakai, and D. Lavoie, 1999, Elasticity of marine sediments: Rock physics modeling: Geophysical Research Letters, **26**, 1781–1784, doi: 10.1029/1999GL900332.

Ghose, R., 2010, 8. Estimating in situ horizontal stress in soil using time-lapse Vs measurements, *in* R. D. Miller, J. H. Bradford, and K. Holliger, eds., Geophysical development series No. 15, Advances in near-surface seismology and ground-penetrating radar: SEG, 131–152.

Ghose, R., 2012, A microelectromechanical system digital 3C array seismic cone penetrometer: Geophysics, **77**, no. 3, WA99–WA107, doi: 10.1190/geo2011-0266.1.

Ghose, R., J. Brouwer, and V. Nijhof, 1996, A portable S-wave vibrator for high-resolution imaging of the shallow subsurface: 58th Annual International Conference and Exhibition, EAGE, Extended Abstracts, M037, doi: 10.3997/2214-4609.201408721.

Ghose, R., and J. Goudswaard, 2004, Integrating S-wave seismic-reflection data and cone penetration test data using a multiangle multiscale approach: Geophysics, **69**, 440–459, doi: 10.1190/1.1707064.

Graves, R. W., 1996, Simulating seismic wave propagation in 3D elastic media using staggered-grid finite differences: Bulletin of the Seismological Society of America, **86**, 1091–1106, doi: 10.1785/BSSA0860041091.

Hansen, P., 2010, Discrete inverse problems: Insight and algorithms: SIAM.

Hardin, B. O., and W. L. Black, 1966, Sand stiffness under various triaxial stresses: Journal of the Soil Mechanics Foundation Division, **92**, 27–42, doi: 10.1061/JSFEAQ.0000865.

Herckenrath, D., 2012, Informing groundwater models with near-surface geophysical data: Ph.D. thesis, Technical University of Denmark.

Irnaka, T. M., R. Brossier, L. Métivier, T. Bohlen, and Y. Pan, 2022, 3-D multicomponent full waveform inversion for shallow-seismic target: Ettlingen Line case study: Geophysical Journal International, **229**, 1017–1040, doi: 10.1093/gji/ggab512.

Ishihara, K., 1982, Evaluation of soil properties for use in earthquake response analysis: Proceedings of the International Symposium on Numerical Models in Geomechanics, 237–259.

Jamiolkowski, M., and D. C. F. Lo Presti, 1994, Validity of in situ tests related to real behavior: Proceedings of the 13th International Conference on Soil Mechanics and Foundation Engineering, 51–55.

Kawasaki, Y., S. Minato, and R. Ghose, 2024, Subsoil density field reconstruction through 3-D FWI: A systematic comparison between vertical- and horizontal-force seismic sources: Geophysical Journal International, **236**, 727–747, doi: 10.1093/gji/ggad445.

Köhn, D., D. De Nil, A. Kurzmann, A. Przebindowska, and T. Bohlen, 2012, On the influence of model parametrization in elastic full waveform tomography: Geophysical Journal International, **191**, 325–345, doi: 10.1111/j.1365-246X.2012.05633.x.

Konishi, C., T. Ishizawa, T. Danjo, and N. Sakai, 2015, S-wave velocity monitoring during an artificial rainfall experiment using large scale rainfall simulator: Near Surface Geoscience 2015 21st European Meeting of Environmental and Engineering Geophysics.

Konstantaki, L. A., R. Ghose, D. Draganov, and T. Heimovaara, 2016, Wet and gassy zones in a municipal landfill from P- and S-wave velocity fields: Geophysics, **81**, no. 6, EN75–EN86, doi: 10.1190/geo2015-0581.1.

Lam, L., D. Fredlund, and S. Barbour, 1987, Transient seepage model for saturated–unsaturated soil systems: A geotechnical engineering approach: Canadian Geotechnical Journal **24**, 565–580, doi: 10.1139/t87-071.

Liberty, L. M., and G. M. Gribler, 2014, Shear wave seismic velocity profiling and depth to water table — Earthquake site response measurements for Valley County, Idaho: Technical Report, Idaho Geological Survey.

Likos, W. J., N. Lu, and J. W. Godt, 2014, Hysteresis and uncertainty in soil water-retention curve parameters: Journal of Geotechnical and Geoenvironmental Engineering, **140**, 04013050, doi: 10.1061/(ASCE)GT.1943-5606.0001071.

Locci-Lopez, D., and J. M. Lorenzo, 2023, Seepage — Induced pore pressure variations beneath an earthen levee measured with a novel seismic tool: Geosciences, **13**, 20, doi: 10.3390/geosciences13010020.

Lorenzo, J. M., J. Hicks, and E. E. Vera, 2014, Integrated seismic and cone penetration test observations at a distressed earthen levee: Marrero, Louisiana, USA: Engineering Geology, **168**, 59–68, doi: 10.1016/j.enggeo.2013.10.019.

Ng, C. W. W., and Q. Shi, 1998, A numerical investigation of the stability of unsaturated soil slopes subjected to transient seepage: Computers and Geotechnics, **22**, 1–28, doi: 10.1016/S0266-352X(97)00036-0.

Nuth, M., and L. Laloui, 2008, Effective stress concept in unsaturated soils: Clarification and validation of a unified framework: International Journal for Numerical and Analytical Methods in Geomechanics, **32**, 771–801, doi: 10.1002/nag.645.

Pan, Y., L. Gao, and T. Bohlen, 2019, High-resolution characterization of near-surface structures by surface-wave inversions: From dispersion curve to full waveform: Surveys in Geophysics, **40**, 167–195, doi: 10.1007/s10712-019-09508-0.

Pasquet, S., L. Bodet, A. Dhemaied, A. Mouhri, Q. Vitale, F. Rejiba, N. Flipo, and R. Guérin, 2015, Detecting different water table levels in a shallow aquifer with combined P-, surface and SH-wave surveys: Insights from V_P/V_S or Poisson's ratios: Journal of Applied Geophysics, **113**, 38–50, doi: 10.1016/j.jappgeo.2014.12.005.

Pol, J. C., W. Kanning, and S. N. Jonkman, 2021, Temporal development of backward erosion piping in a large-scale experiment: Journal of Geotechnical and Geoenvironmental Engineering, **147**, 04020168, doi: 10.1061/(ASCE)GT.1943-5606.0002415.

Qin, L., J. H. Steidl, H. Qiu, N. Nakata, and Y. Ben-Zion, 2022, Monitoring seasonal shear wave velocity changes in the Top 6 m at Garner Valley in Southern California with borehole data: Geophysical Research Letters, **49**, e2022GL101189, doi: 10.1029/2022GL101189.

Richards, L. A., 1931, Capillary conduction of liquids through porous mediums: Physics, **1**, 318–333, doi: 10.1063/1.1745010.

Robinson, D., A. Binley, N. Crook, F. Day-Lewis, T. Ferré, V. Grauch, R. Knight, M. Knoll, V. Lakshmi, R. Miller, J. Nyquist, L. Pellerin, K. Singha, and L. Slater, 2008, Advancing process-based watershed hydrological research using near-surface geophysics: A vision for, and review of, electrical and magnetic geophysical methods: Hydrological Processes, **22**, 3604–3635, doi: 10.1002/hyp.6963.

Romero-Ruiz, A., N. Linde, L. Baron, S. G. Solazzi, T. Keller, and D. Or, 2021, Seismic signatures reveal persistence of soil compaction: Vadose Zone Journal, **20**, e20140, doi: 10.1002/vzj2.20140.

Rücker, C., T. Günther, and F. M. Wagner, 2017, pyGIMLi: An open-source library for modelling and inversion in geophysics: Computers & Geosciences, **109**, 106–123, doi: 10.1016/j.cageo.2017.07.011.

Santamarina, J., and G. Cascante, 1996, Stress anisotropy and wave propagation: A micromechanical view: Canadian Geotechnical Journal, **33**, 770–782, doi: 10.1139/t96-102-323.

Sawangsuriya, A., T. B. Edil, and P. J. Bosscher, 2009, Modulus-suction-moisture relationship for compacted soils in postcompaction state: Journal of Geotechnical and Geoenvironmental Engineering, **135**, 1390–1403, doi: 10.1061/(ASCE)GT.1943-5606.0000108.

Saxena, S. K., A. S. Avramidis, and K. R. Reddy, 1988, Dynamic moduli and damping ratios for cemented sands at low strains: Canadian Geotechnical Journal, **25**, 353–368, doi: 10.1139/t88-036.

Shen, J., J. M. Crane, J. M. Lorenzo, and C. D. White, 2016, Seismic velocity prediction in shallow (< 30 m) partially saturated, unconsolidated sediments using effective medium theory: Journal of Environmental and Engineering Geophysics, **21**, 67–78, doi: 10.2113/JEEG21.2.67.

Solazzi, S. G., L. Bodet, K. Holliger, and D. Jougnot, 2021, Surface-wave dispersion in partially saturated soils: The role of capillary forces: Journal of Geophysical Research: Solid Earth, **126**, e2021JB022074, doi: 10.1029/2021JB022074.

Stokoe, K. H., S. H. Lee, and D. P. Knox, 1985, Shear moduli measurements under true triaxial stresses: Proceedings of Advances in the Art of Testing Soils under Cyclic Conditions: Geotechnical Engineering Division, 166–185.

Suzaki, A., S. Minato, and R. Ghose, 2018, Inversion of soil-water characteristic curve in unsaturated soil embankment using the underlying physics of S-wave and integrated geophysics: 88th Annual International Meeting, SEG, Expanded Abstracts, 4748–4752, doi: 10.1190/segam2018-2995904.1.

Suzaki, A., S. Minato, R. Ghose, C. Konishi, and N. Sakai, 2017, Modelling time-lapse shear-wave velocity changes in an unsaturated soil embankment due to water infiltration and drainage: First Break, **35**, 69–78, doi: 10.3997/1365-2397.35.8.89811.

Tran, K. T., M. Mirzanejad, M. McVay, and D. Horhota, 2019, 3-D time-domain Gauss–Newton full waveform inversion for near-surface site characterization: Geophysical Journal International, **217**, 206–218, doi: 10.1093/gji/ggz020.

Van Genuchten, M. T., 1980, A closed-form equation for predicting the hydraulic conductivity of unsaturated soils: Soil Science Society of America Journal, **44**, 892–898, doi: 10.2136/sssaj1980.03615995004400050002x.
Velea, D., F. D. Shields, and J. M. Sabatier, 2000, Elastic wave velocities in partially saturated Ottawa sand: Experimental results and modeling: Soil Science Society of America Journal, **64**, 1226–1234, doi: 10.2136/sssaj2000.6441226x.
West, M., and W. Menke, 2000, Fluid-induced changes in shear velocity from surface waves: 13th EEGS Symposium on the Application of Geophysics to Engineering and Environmental Problems.
Whalley, W., M. Jenkins, and K. Attenborough, 2012, The velocity of shear waves in unsaturated soil: Soil and Tillage Research, **125**, 30–37, doi: 10.1016/j.still.2012.05.013.
Whalley, W. R., M. Jenkins, and K. Attenborough, 2011, The velocity of shear waves in saturated soil: Soil Science Society of America Journal, **75**, 1652–1657, doi: 10.2136/sssaj2010.0449.
Whiteley, J., J. Chambers, S. Uhlemann, J. Boyd, M. Cimpoiasu, J. Holmes, C. Inauen, A. Watlet, L. Hawley-Sibbett, C. Sujitapan, R. T. Swift, and J. M. Kendall, 2020, Landslide monitoring using seismic refraction tomography — The importance of incorporating topographic variations: Engineering Geology, **268**, 105525, doi: 10.1016/j.enggeo.2020.105525.
Whiteley, J., J. Chambers, S. Uhlemann, P. Wilkinson, and J. Kendall, 2018, Geophysical monitoring of moisture-induced landslides: A review: Reviews of Geophysics, **57**, 106–145, doi: 10.1029/2018RG000603.
Williams, R. A., W. J. Stephenson, J. K. Odum, and D. M. Worley, 2003, Seismic velocities from high-resolution surface-seismic imaging at six ANSS sites near Memphis, Tennessee: USGS Open-File Report 2003-218.
Yagisawa, J., M. van Damme, J. C. Pol, and J. D. Bricker, 2019, Verification of a predictive formula for critical shear stress with large scale levee erosion experiment: 11th ICOLD European Club Symposium, Greek Committee on Large Dams.
Zimmer, M. A., M. Prasad, G. Mavko, and A. Nur, 2007, Seismic velocities of unconsolidated sands: Part 1 — Pressure trends from 0.1 to 20 MPa: Geophysics, **72**, no. 1, E1–E13, doi: 10.1190/1.2399459.

Biographies and photographs of the authors are not available.